

## Predicting laser weld reliability with stochastic reduced-order models

John M. Emery<sup>1,\*†</sup>, Richard V. Field, Jr.<sup>1</sup>, James W. Foulk III<sup>2</sup>, Kyle N. Karlson<sup>2</sup>  
and Mircea D. Grigoriu<sup>3</sup>

<sup>1</sup>*Sandia National Laboratories, Albuquerque, New Mexico*

<sup>2</sup>*Sandia National Laboratories, Livermore, CA, USA*

<sup>3</sup>*Cornell University, Ithaca, NY, USA*

### SUMMARY

Laser welds are prevalent in complex engineering systems and they frequently govern failure. The weld process often results in partial penetration of the base metals, leaving sharp crack-like features with a high degree of variability in the geometry and material properties of the welded structure. Accurate finite element predictions of the structural reliability of components containing laser welds requires the analysis of a large number of finite element meshes with very fine spatial resolution, where each mesh has different geometry and/or material properties in the welded region to address variability. Traditional modeling approaches cannot be efficiently employed. To this end, a method is presented for constructing a surrogate model, based on stochastic reduced-order models, and is proposed to represent the laser welds within the component. Here, the uncertainty in weld microstructure and geometry is captured by calibrating plasticity parameters to experimental observations of necking as, because of the ductility of the welds, necking – and thus peak load – plays the pivotal role in structural failure. The proposed method is exercised for a simplified verification problem and compared with the traditional Monte Carlo simulation with rather remarkable results.

Copyright © 2015 John Wiley & Sons, Ltd.

Received 17 November 2014; Revised 28 March 2015; Accepted 9 April 2015

KEY WORDS: laser welds; structural reliability; stochastic reduced-order models; Monte Carlo simulation

### 1. INTRODUCTION

Laser welds are used in many applications in the aerospace, automotive, computer, and electronics industries. Because laser welding does not require physical contact, it is inherently well-suited for small-scale applications near heat sensitive materials [1]. Often, these fine-scale joints play a pivotal role in structural failure and, thus, they have an important role in overall system reliability. Laser welds are formed by generating enough heat with the focused energy of the laser beam to melt base metals. Designs frequently require partial penetrations with a significant unwelded ligament, as shown in Figure 1(a). The resulting geometric features of the weldment – penetration depth, surface width, and so on – and the material properties are highly variable and random. In addition to the obvious stress concentration at the root of the partial penetration weld, significant porosity can arise that can play a role in weld behavior [2, 3]. In very ductile alloys like grade 304L austenitic stainless steel (SS), the geometry and porosity of the weld interact to create a very complex necking process that dominates the strength of the weld, eventually leading to fracture. This gives rise to significant variability in the structural response of the welded component as can be seen from the tensile coupon data plotted in Figure 1(b). Forty tensile specimens were cut from butt welded plates resulting in a

\*Correspondence to: John M. Emery, P.O. Box 5800 MS 0346, Albuquerque, New Mexico 87185-0346.

†E-mail: jmemery@sandia.gov

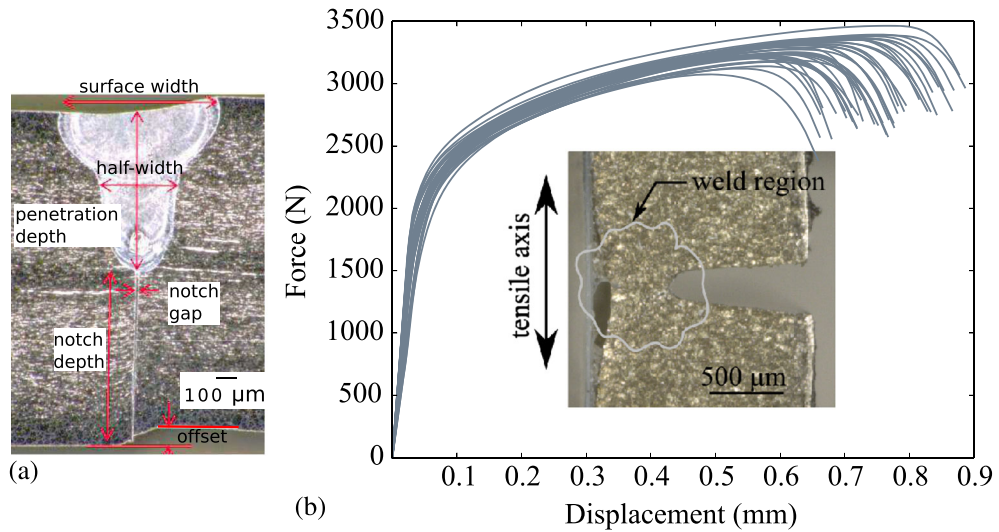


Figure 1. (a) A laser butt weld with variable geometry and (b) the observed force-displacement response under tension (photos and data from [2]).

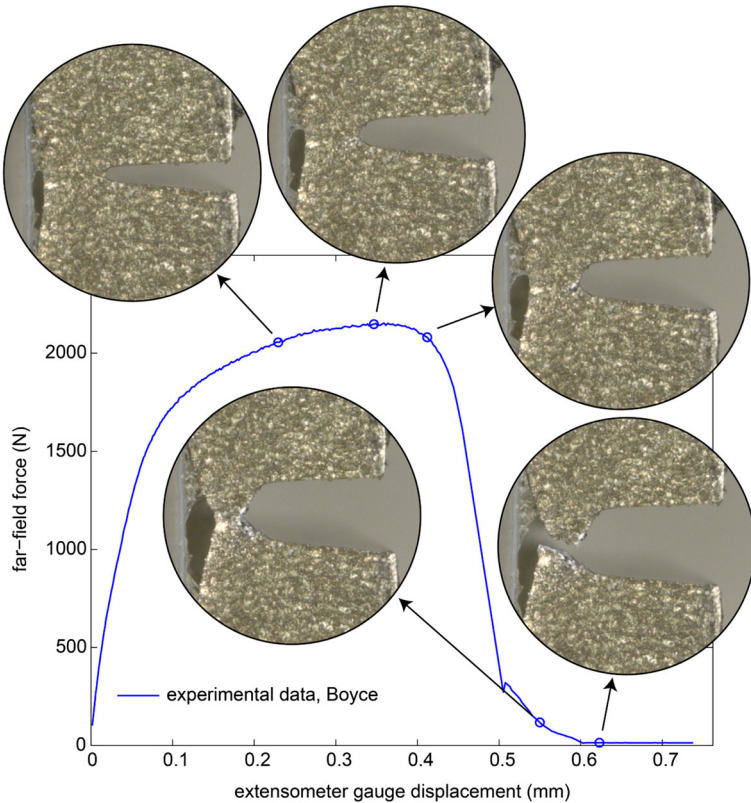


Figure 2. The force-displacement curve illustrating the necking of a laser weld under far-field tension. The appearance of new surface area does not occur until the load has significantly dropped.

partial penetration laser weld at the specimen midplanes. The specimens were nominally identical, but the peak load varies by 13% and the strain at peak load varies by 59%. Note that, because of the eccentricity caused by partial penetration, the loaded specimen exhibits bending and these curves do not resemble material stress-strain relations.

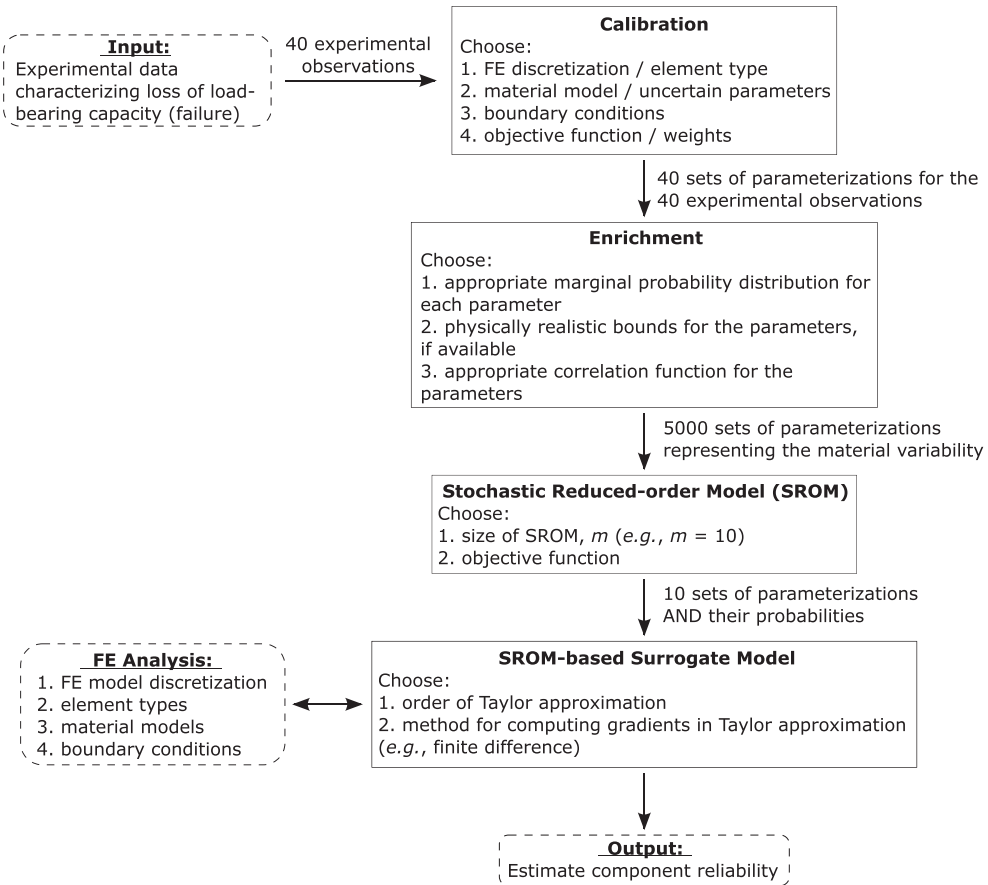


Figure 3. Flowchart illustrating the proposed methodology for estimating component reliability because of laser weld failure.

Figure 2 illustrates the complex deformation process observed throughout tensile loading with significant cross-section reduction and fracture occurring only after the load was reduced to approximately 7% of peak. The figure makes clear that for 304L SS, the load carrying capacity is dominated by necking with failure immediately following the onset of the geometric instability. It is not uncommon to see local plastic strains on the order of 200–300%. The spatial resolution necessary to capture precisely the response of the tensile coupons illustrated in Figure 2 with detailed, three-dimensional finite element (FE) models is intractable because of the disparate length scales at play. The penetration depth of the laser welds of interest is typically on the order of hundreds of microns while the relevant length scale of the system containing them may be on the order of meters.

In this article, we present a methodology to rationally capture the material and processing variability associated with laser welding and propagate this uncertainty to prediction of component reliability. We focus on failure caused by sub-millimeter, partial-penetration laser welds in 304L SS where the local deformations preceding failure are very large and failure is governed by loss of load-bearing capacity of the weld, not crack propagation. Further, attention is restricted to quasi-static loading at room temperature. The method outlined in this article captures the relevant physics and uncertainty with tractable computational effort. This requires methods to efficiently discretize the stochastic space and reduce the computational complexity of the problem. For the former, we employ stochastic reduced-order models (SROMs) [4, 5]. For the latter, a surrogate model, built with piecewise continuous polynomial fits that approximate the output of interest, is constructed based on the SROM [6]. The proposed method is exercised for a simple, welded tensile coupon and compared with the traditional Monte Carlo simulation (MCS) with rather remarkable results.

The organization for the remainder of this article is as follows. In Section 2, we outline the proposed method and describe the workflow as seen by the analyst. In Section 3, the details of the calibration process are discussed including the FE model and the material test data that were used for calibration. Section 4 discusses the available data and the process used to extract as much meaning from the data as physically possible. Section 5 describes the construction of an SROM for the uncertain material parameters that describe the 304L SS laser weld constitutive response. Section 6 defines the surrogate model, details its construction and provides a numerical example that provides verification for the overall methodology.

## 2. METHODOLOGY

The objective of this work is to provide a rational and tractable engineering solution to the problem of predicting structural reliability of a laser welded component. Figure 3 illustrates the proposed methodology with a flowchart. The three dashed-line boxes represent elements of the current practice of computational modeling for weld reliability and show the input data, the FE analysis procedure, and the output. In the absence of our approach, an analyst would calibrate their constitutive model to materials characterization tests and perform FE calculations informed by the available experimental data. Typically, the available data are limited to two or three characterization tests and the material properties of the weld are assumed to be identical to the base material. The calculations are often coarse enough that they do not fully resolve the local deformation and they employ a criterion for failure, e.g., a maximum allowable equivalent plastic strain. Further, these calculations may include a parametric study or MCS with limited samples and assumed probability distributions, but we assume that they are detailed enough and complex enough that generalized, large-scale MCS is intractable. Hence, the output from these calculations would lack sufficient fidelity for accurate estimates of component reliability, especially when high reliability requirements exist. We propose to improve this without increasing the computational cost and by carefully modeling the deformation process to avoid arbitrary failure criteria by the process outlined with the solid-line boxes. In the following, we introduce the technical highlights of each solid-line box, leaving the details to the subsequent sections.

We calibrate to a robust set of experimental data that characterizes failure of a sub-component of importance. In the calibration box, constitutive parameters of a three-dimensional FE model of the sub-component are chosen to fit its response to the available data; in our example, we fit to the experimentally observed force-displacement data for the forty laser-welded tensile coupons, shown in Figure 1(b) [2]. Because the tensile coupons contain the eccentricity of the partial penetration welds, the constitutive parameters do not represent material properties. Three-dimensional FE analysis is required to capture the global necking process that was previously identified as the failure mechanism. Additional decisions are required during calibration including boundary conditions, element formulation, and constitutive model. In the present case, the calibration is used to account for all material uncertainty so that the choice of constitutive model emits all possible stochastic parameters in the problem. The analyst is required to decide which parameters to include in the stochastic dimension of the problem based on model sensitivities.

In this work, we used the Bamman, Chiesa, and Johnson plasticity model (BCJ\_MEM) that uses von Mises equivalent stress for the yield parameter and evolves the yield surface with a two-parameter, hardening-minus-recovery model [7, 8]. The FE calculations were decidedly insensitive to the elastic parameters in the constitutive model and, as previously mentioned, rate and temperature effects were neglected. Hence, the stochastic dimension in this work is three and contains the plasticity parameters, which are as follows: (i) the initial yield strength; (ii) the recovery term; and (iii) the hardening term. These are collected in the random vector  $\Theta \in \mathbb{R}^d$  where  $d = 3$  in this article. The method readily extends to uncertainties other than uncertain constitutive parameters, e.g., geometric parameters.

The enrichment box describes a process through which the outcome of the forty calibrations are fit to marginal distributions and correlations, observing physical constraints, to enhance the population

of observations. The choice of marginal distributions and correlations are engineering decisions directly analogous to choosing a particular functional form to represent the constitutive behavior of material response. Translational random vectors are used to generate a set of  $n = 5000$  independent samples of the random vector  $\Theta$  [9]. This process is necessary because the construction of the SROM involves choosing the optimal sub-collection from a very large collection of equally likely samples<sup>‡</sup>. If the collection to choose from is too small, the optimization routine provides a poor representation of the data. Ideally, there would be sufficient data available to avoid the necessity of enrichment. This is impractical for the current example because extensive weld coupon tensile tests are cost prohibitive.

The stochastic reduced-order model box represents the construction of the SROM. The SROM is a discrete approximate for the uncertain constitutive parameters  $\Theta$  with samples carefully chosen to preserve their statistics. To construct an SROM, the analyst chooses the size of the reduced model,  $m \ll n$ . This decision is primarily based on the cost of the component simulations required to construct the SROM-based surrogate, which uses at least as many FE runs as there are samples  $m$  in the SROM. Secondarily,  $m$  is chosen based on the desired fidelity of the reduced-order model because it can be shown that the SROM is convergent with refinement [6]. Thus, a judicious choice for the size of the SROM is necessary. We have constructed 10-sample, 20-sample, 40-sample, and 80-sample SROMs and report the findings in Sections 5 and 6. The other user-supplied input for the SROM box describes how the SROM relates to the uncertain parameters. Choices include the number of higher-order moments to preserve and weights to allow user control over various aspects of the model.

To this point, the focus has been on developing a model for the uncertain constitutive parameters to be used for component calculations. For simulation of the component response, we use an SROM-based surrogate model shown in the SROM-based Surrogate Model box<sup>§</sup>. The surrogate is a piecewise constant or piecewise linear response surface that maps samples of  $\Theta$  to the quantity of interest, e.g., force-displacement of a weld coupon. The piecewise linear model uses a first-order Taylor expansion in  $\Theta$  where the expansion points are chosen based on the SROM samples. The coefficients of the Taylor expansion are approximated using FE calculations. For this, an FE calculation is required at each expansion point and additionally for each coordinate of the uncertain vector to compute the gradient by forward finite difference. For example, an SROM with  $m = 10$  samples and stochastic dimension  $d = 3$ , the number of FE calculations required to construct the surrogate model is  $m(d + 1) = 40$ .

In this article, we illustrate our methodology with the tensile coupon itself, i.e., the component and sub-component are the same. Once the surrogate is constructed, there are no further FE calculations necessary. MCS is conducted by evaluating the surrogate's response surface to map the  $n = 5000$  samples of  $\Theta$  to force-displacement response (virtually instantaneously). As discussed in the our introduction, failure for this sub-component can be predicted by the peak force in the force-displacement response. Hence, for illustration, the force-displacement curves are post-processed to extract peak force and its cumulative probability distribution is plotted for estimation of component reliability. For verification, we also compute the response of the tensile coupon with FE calculations for the  $n = 5000$  samples of  $\Theta$  and compare with the results from the SROM-based surrogate.

<sup>‡</sup>Alternately, the SROM could be constructed directly from the marginal distributions and correlations; however, we choose to use a large number of samples to illustrate the method on the occasion of the presence of a large set of experimental data and to facilitate our MCSs.

<sup>§</sup>Other model order reduction methods, e.g., proper orthogonal decomposition and proper generalized decomposition, strive for computational savings through reduction of the computational model used to solve the differential equations [10, 11]. These require significant modification of existing FE codes. In contrast, an SROM strives to reduce the stochastic dimension of inputs to the FE code and the SROM-based surrogate acts as a response surface for the output quantity of interest. The SROM approach is minimally invasive to existing codes and was implemented with Python wrapping the quasi-static FE code. There are other well-established sampling methods for uncertainty quantification of which the SROM-based method is most similar to stochastic collocation [12, 13]. Detailed comparison between these and our choice of the SROM-based surrogate is included in a manuscript written by a subset of the authors of this paper and currently under review [14].

### 3. CALIBRATION

In this section, we outline the details for calibration of the constitutive model parameters to the available data. Tensile data is used from 40 nominally identical tensile coupons that were manufactured as described in [2] and shown in Figure 1(b). The tensile coupons were cut from butt welded plates resulting in a partial penetration laser weld at the specimen midplanes. We first describe the three-dimensional FE model used for calibration. Then, details are provided on the optimization used to match the FE model response to the experimental data. The outcome of the calibration is 40 sets of material parameters that parameterize the observed uncertainty in the laser welds of these experiments. In practice, the analyst should perform this calibration for tensile specimens with the intended material form and welded with the appropriate weld schedule suited for their application, as these strongly affect the performance of the resulting welds.

#### 3.1. Three-dimensional finite element model

The BCJ\_MEM material model [7] is used for both the weld region and the bulk material away from the weld; however, only the parameters for the weld region were varied for calibration. We idealize the plastic flow to be governed by a yield surface having the form

$$\sigma_y = y + \kappa \quad (1)$$

where  $y$  is the initial yield strength and  $\kappa$  is the isotropic hardening. For rate-independent flow with no static recovery, the evolution of  $\kappa$  is expressed as

$$\kappa(\epsilon_p) = \frac{h}{r} [1 - \exp(-r\epsilon_p)] \quad (2)$$

with  $h$  the linear hardening term,  $r$  the recovery term, and  $\epsilon_p$  the equivalent plastic strain. Only the initial yield strength  $y$ , the recovery term  $r$ , and the hardening term  $h$  of the weld region are included as design variables in the objective function during optimization. The plasticity parameters for the base material were estimated through prior work [2] and held constant. We assume the elastic properties are fixed with modulus of elasticity = 180 GPa and Poisson's ratio = 0.27.

The geometry of the FE model replicates the nominal dimensions of the free-span tensile coupons,  $38.1 \times 6.35 \times 1.6$  mm, accounting for planes of symmetry, and has the nominal 0.76 mm weld penetration. This FE mesh contains 6440 linear hexahedral elements. Appropriate kinematic boundary conditions are used for the planes of symmetry and the loading is applied by axial displacement. The finite element calculations to fit the design variables were completed with Adagio, Sandia's SIERRA Solid Mechanics quasi-static FE code [15].

The mesh was checked for numerical convergence with two uniform mesh refinements by successively halving the element size. The computed force-displacement response up to peak load remains unchanged with refinement (Figure 4(a)). Deviations in the force-displacement curves after peak load stem from sharper gradients and mesh distortion. The boundary value problem is well-posed and regularization is not needed [16]. The far-field displacement shown in Figure 4 and Figure 1(b) is collected from a 25.4 mm extensometer centered about the weld. This is accomplished in the FE model by forcing the mesh to have a set of nodes centered about the weld at the extensometer gage length of 25.4 mm. We note that the mesh refinement study was conducted on the lower bound, median, and upper bound of the measured force-displacement curves. Because the force-displacement curves are convergent for parameters that span the experimental data, we conclude that model parameters derived from the calibration process are independent of the discretization.

We are required to idealize the blunting process that occurs at the root of the weld to avoid remeshing and mapping of internal state variables. Given that 304L SS permits substantial crack-tip blunting, we seek to capture the effect of the weld partial penetration without resolving a reentrant corner. As such, we idealize the root of the weld with a smooth notch as can be seen in Figure 5. The notch and discretization were carefully selected to mitigate and resolve the local deformations that occur at the notch tip. A specific investigation of notch radius is illustrated in Figure 4(b). From inspection of the deformed shape of the FE models for this study, we found that for the initial notch

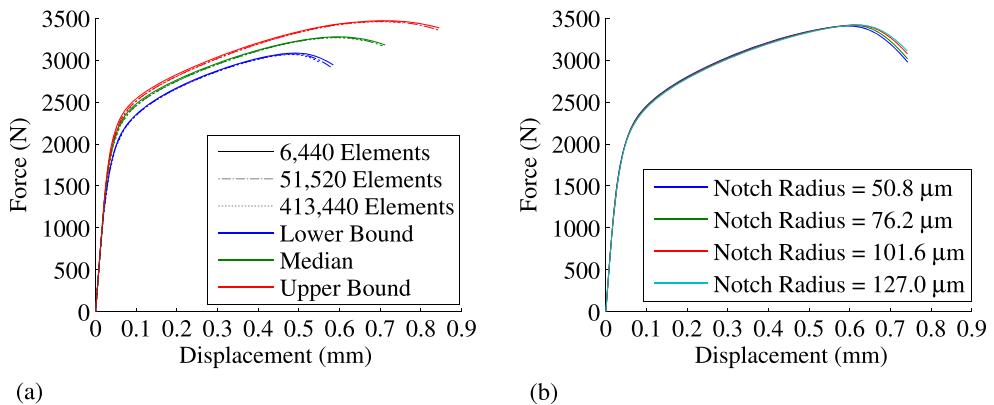


Figure 4. Force-displacement demonstrating (a) mesh convergence and (b) convergence in peak load with varying notch radii.

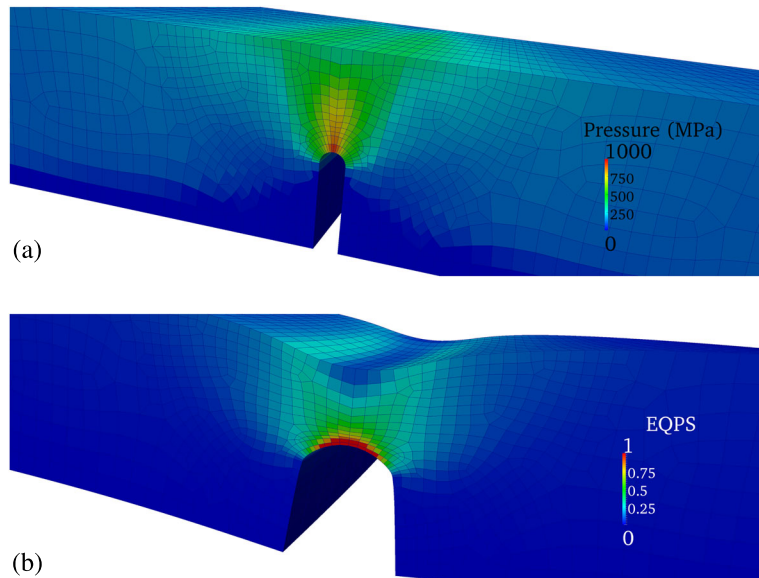


Figure 5. Contour plots presented on a longitudinal cross-section along the mid-plane of the coupon of (a) the pressure field and (b) the equivalent plastic strain (average of integration points) on the deformed shape. The tensile axis is in the y-direction (approximately left-right, across the page). Both the stresses and the deformations are smooth and well-resolved.

radii of 50.8, 76.2, 101.6, and 127.0  $\mu\text{m}$ , the notch radii at necking became 222.7, 257.0, 290.3, and 330.2  $\mu\text{m}$ , respectively. Based on these findings, a notch radius of 76.2  $\mu\text{m}$  was selected for the calibration process.

In addition to examining the far-field reaction forces that stem from the applied displacement, we also examine the fields around the notch. The fields for pressure and the equivalent plastic strain are shown in Figure 5(a) and (b), respectively. The constant-pressure element formulation used here results in a smooth pressure under large isochoric motions. The mid-plane of the specimen is shown because the peak plastic strains reside at the mid-plane. Unlike the free surface where isochoric motions can be accommodated through in-plane and out-of-plane contractions, the mid-plane must contract to the extent it is elongated. We observe smooth and resolved fields during the evolution of the neck. Although we have neglected the residual stresses that result from the welding process, the widespread plasticity noted in Figure 5(b) ensures that those initial stresses would be well redistributed. In addition, the effective stress in the notch is on the order of three times the

initial yield stress. Redistribution and hardening mitigates the effects of residual stresses on the necking process.

### 3.2. Optimization

The optimization code DAKOTA [17] was used to iteratively select sets of the initial yield strength  $y$ , the recovery term  $r$ , and the hardening term  $h$  to fit the response of the FE calculation to the measured force-displacement curves of the welded coupons. Figure 6(a) illustrates the force-displacement curves from the experimental measurements. First, a derivative-free, global optimization algorithm was employed to select parameters for the upper bound, the median, and lower bound of the data. A weighting function that emphasized the plateau and necking regions of the force-displacement curves was employed and large, non-physical bounds were supplied with relatively loose tolerances. These fits were refined with a secant-based, least-squares algorithm. Subsequently, with parameter bounds informed from the global optimizations, the least squares algorithm was used to calibrate the remaining 37 curves. The outcome is shown in Figure 6(b).

As indicated in Figure 6(b), the calibration process retains the general character of the experimental data. For each test, a single yield stress  $y$ , hardening  $h$ , and recovery term  $r$  was optimized

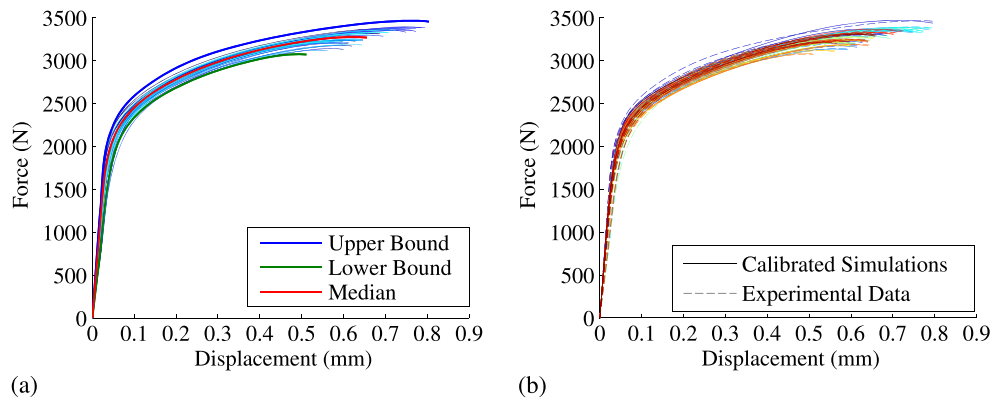


Figure 6. (a) The measured data highlighting the upper and lower bounds and the median and (b) the results from calibration. The post-peak response has been removed.

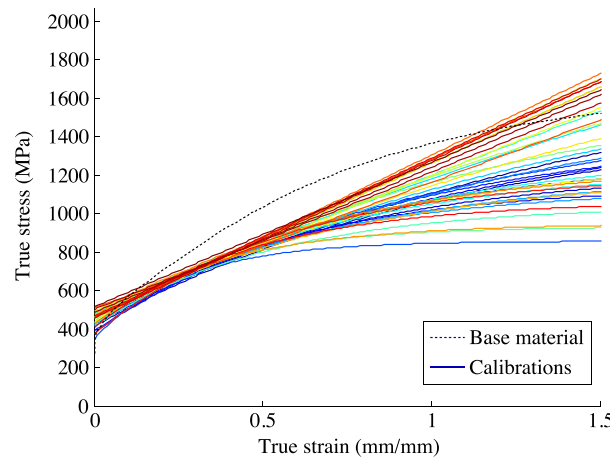


Figure 7. Generated true stress-strain curves from 40 calibrations. The yield strength  $y$  intersects the independent axis while the linear hardening  $h$  and recovery  $r$  specify the asymptote  $\frac{h}{r}$  with increasing equivalent plastic strain  $\epsilon_p$ . The calibrated fits are contrasted against the model employed for the base material.

to capture both the plateau and the load/displacement at necking. Using each of the 40 fits, we can generate a calibrated stress-strain response through Equation (2) and compare with the stress-strain response of the base material, plotted in Figure 7. In many cases, the fit yielded linear hardening ( $r = 0$ ). In general, the calibrated curves do tend to have a higher yield stress and less hardening than the base material. Although an increased yield strength is consistent with prior work [2], the calibrated yield strength is in excess of the reported values. Of greater relevance is that for plastic strains below one, the calibrated weld material is softer than the base material. We have attempted to capture both geometric variability and deformation mechanisms prior to global necking through an effective, calibrated response.

#### 4. ENRICHMENT

Let  $\{\boldsymbol{\theta}_k, k = 1, \dots, q = 40\}$  denote the available data, where each  $\boldsymbol{\theta}_k = (y_k, r_k, h_k)'$  is a vector containing calibrations of initial yield stress, recovery term, and hardening term defined by Equations (1) and (2); we assume that the  $\{\boldsymbol{\theta}_k\}$  are independent samples of a random vector  $\boldsymbol{\Theta} = (Y, R, H)'$  where we have replaced  $(y, r, h)$  with  $(Y, R, H)$  to indicate the latter are random variables. In most cases, the number of measurements  $q$  is small and insufficient to construct an SROM for  $\boldsymbol{\Theta}$ ; we therefore require a method to enrich the available data set. In this section, we develop a non-Gaussian translation model for  $\boldsymbol{\Theta}$  [18, Section 3.1] that can be used for this purpose. This approach has several advantages that make it attractive for problems of this type: (i) one can match any non-Gaussian marginal distribution; (ii) with some exceptions, one can also match the covariance function of the non-Gaussian vector; (iii) the method is conceptually simple; and (iv) the generation of random samples via MCS is straightforward and efficient.

##### 4.1. Model definition

Let  $\mathbf{G} = (G_1, G_2, G_3)'$  be a Gaussian random vector with coordinates satisfying  $E[G_k] = 0$ ,  $\text{Var}[G_k] = 1$ , and  $\rho_{kl} = E[G_k G_l]$ ,  $k, l = 1, 2, 3$  where  $E[A]$  and  $\text{Var}[A]$  denote the expected value and variance of random variable  $A$ , respectively. Our proposed model for  $\boldsymbol{\Theta}$  used to enrich the available data set is defined as a simple nonlinear transformation of  $\mathbf{G}$ , called a translation random vector [9, 18]. Let  $\mu_k = E[\Theta_k]$  and  $\sigma_k^2 = \text{Var}[\Theta_k]$ ; the form of this transformation is given by

$$\Theta_k = f_k(G_k) = F_k^{-1} \circ \Phi(G_k), \quad (3)$$

where each  $F_k$  is a cumulative distribution function CDF and a satisfying

$$\int_{\mathbb{R}} u \, dF_k(u) = \mu_k \quad \text{and} \quad \int_{\mathbb{R}} (u - \mu_k)^2 \, dF_k(u) = \sigma_k^2, \quad (4)$$

and  $\Phi(z) = (2\pi)^{-1/2} \int_{-\infty}^z e^{-u^2/2} \, du$  denotes the XDF of the standard Gaussian random variable. We will refer to  $\mathbf{G}$  as the Gaussian image of  $\boldsymbol{\Theta}$ .

By Equation (3), it can be shown that  $\Theta_k$  has marginal  $F_k$ , that is,  $\Pr(\Theta_k \leq z) = F_k(z)$ ,  $\forall z \in \mathbb{R}$ . Further, the covariance matrix of  $\boldsymbol{\Theta}$  has elements

$$\xi_{kl} = E[(\Theta_k - \mu_k)(\Theta_l - \mu_l)] = E[\Theta_k \Theta_l] - \mu_k \mu_l, \quad (5)$$

where

$$E[\Theta_k \Theta_l] = E[f_k(G_k) f_l(G_l)] = \int_{\mathbb{R}^2} f_k(u) f_l(v) \phi_2(u, v; \rho_{kl}) \, du \, dv, \quad (6)$$

and

$$\phi_2(u, v; \rho) = \frac{1}{2\pi\sqrt{1-\rho^2}} \exp\left(-\frac{u^2 - 2uv\rho + v^2}{2(1-\rho^2)}\right)$$

denotes the joint PDF of two standard Gaussian random variables with correlation  $\rho$ .

#### 4.2. Model calibration

Calibration of our model for  $\Theta$  defined by Equation (3) requires that we define  $\{F_k\}$ , the marginal CFs of  $\Theta$ , as well as  $\{\rho_{kl}\}$ , the covariance matrix of its Gaussian image. We follow four steps:

- (1) Estimate values for  $\{\mu_k\}$  and  $\{\xi_{kl}\}$ , the mean and covariance of  $\Theta$ ;
- (2) Choose a functional form for each CDF  $F_k$ ;
- (3) Estimate values for any parameters associated with each  $F_k$ ; and
- (4) Compute  $\{\rho_{kl}\}$ , the covariance matrix of  $G$ , that will achieve the estimated covariance matrix of  $\Theta$  obtained in step 1.

For step 1, standard statistical estimators can be used. For example,  $(1/q) \sum_{j=1}^q y_j$  provides an estimate for  $\mu_1$ , the mean of the initial yield stress. When choosing the functional form for each CSF, i.e., step 2 of our calibration procedure, statistical as well as physical considerations should be made, that is, each CDF should agree well with the available data but also be consistent with the known physics. For example, Gaussian models should not be used for phenomena that is known to take only positive values or known to lie within a bounded interval. For the data considered here, bounds on the initial yield stress and hardening term defining the constitutive law of the weld material are available. In particular, the initial yield stress takes values between 241 and 620 MPa and the hardening term takes values between 0 and 345 MPa. Further, the recovery term must be non-negative and is extremely unlikely to take values  $>8$ . These bounds are based on expert opinion about the particular weld material, as well as on the results from a series of detailed FE calculations. For the latter, an upper or lower bound on a parameter is obtained when an FE calculation yielded a non-physical result. For applications, sensitivities to these bounds should be carefully considered and the interested reader can find discussion on model selection here [19]. Based on these arguments, we choose CDFs  $F_1$  and  $F_3$  to follow a beta distribution [20, Ch. 25], and  $F_2$  to follow the exponential distribution [21, Ch. 19].

For step 3, standard statistical methods are available, such as the method of moments or method of maximum likelihood [22]. For step 4, given a value for  $\rho_{kl}$ , we solve Equations (5) and (6) to obtain the corresponding value for  $\xi_{kl}$ ; the integration is typically performed numerically. This procedure is repeated for different values of  $\rho_{kl}$  until the interval  $-1 \leq \rho_{kl} \leq 1$  is sufficiently represented, resulting in a collection of pairs  $\{(\rho_{kl}, \xi_{kl})\}$ . Linear interpolation on this collection can then be used to determine  $\rho_{kl}$  for a given specified value for  $\xi_{kl}$ .

Figure 8 illustrates the calibrated model used in this study. The available data,  $\theta_k = (y_k, r_k, h_k)'$ ,  $k = 1, \dots, q = 40$ , are represented by the white vertical bars. The marginal PDFs of  $\Theta$ , that is,  $dF_k(\theta_k)/d\theta_k$ , are also shown and represented by the red curves in the figure. Note that the PDFs are consistent with the bounds assumed for each parameter. Good agreement with the available data is observed in each case.

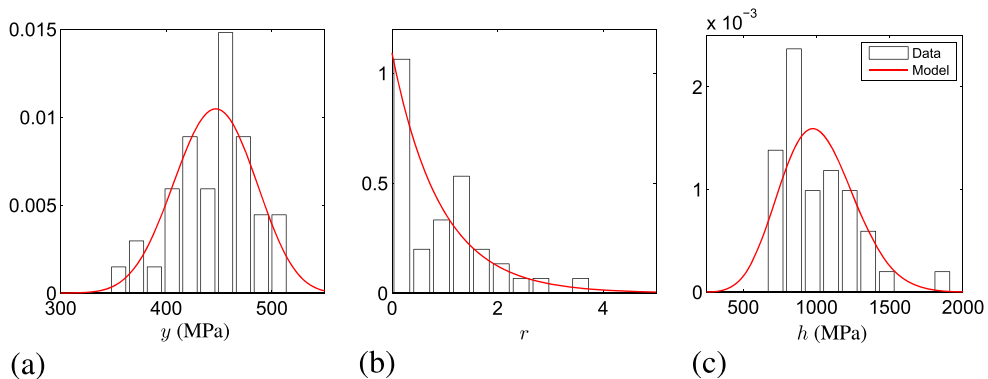


Figure 8. Available data on (a) initial yield stress, (b) recovery term, and (c) hardening term. The red lines denote the marginal PDFs for the translation random vector model used for data enrichment.

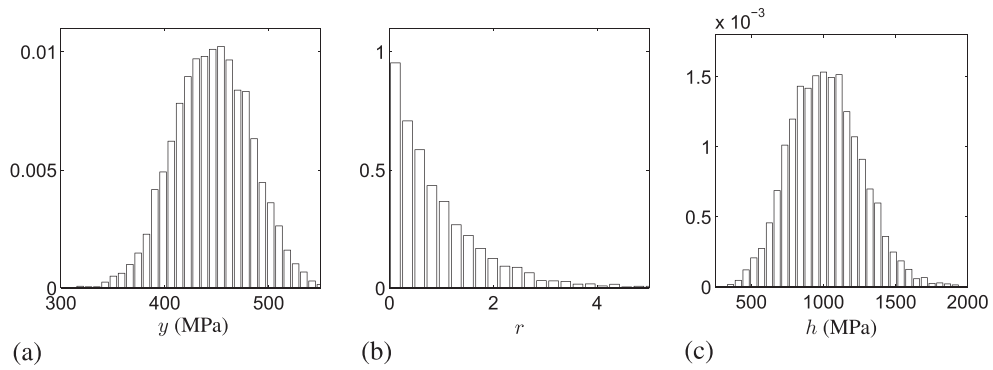


Figure 9. Enriched data set on (a) initial yield stress, (b) recovery term, and (c) hardening term.

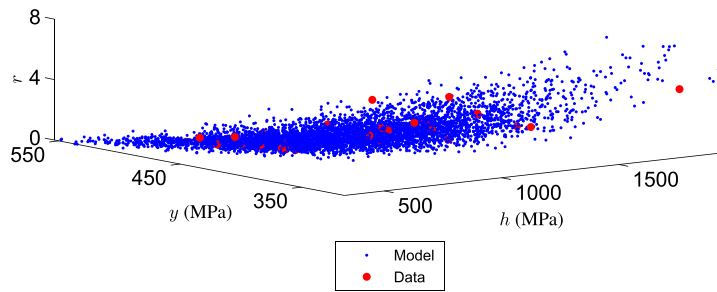


Figure 10. The enriched data set (blue) compared with the available data set (red; enlarged for clarity).

#### 4.3. Sample generation

Once calibrated, creating samples of non-Gaussian random vector  $\Theta$  becomes straightforward and involves two steps, which are as follows:

- (1) Generate  $n$  samples of Gaussian random vector  $\mathbf{G}$  with zero mean, unit variance, and covariance matrix  $\{\rho_{kl}\}$ ; and
- (2) Translate each sample of  $\mathbf{G}$  using Equation (3) to obtain corresponding samples of  $\Theta$ .

For illustration,  $n = 5000$  samples of  $\Theta$  were generated using this procedure; a histogram of these samples is illustrated in Figure 9. Conveniently, the uncertain data is parameterized by three random variables so it lends itself to three-dimensional plotting. Figure 10 illustrates the model versus the available data showing how the model spans the data. In the figure, the available data are plotted with over-sized red dots to make them more visible among the blue model points. This example forms the enriched data set that is used in the following section to construct an SROM for  $\Theta$ .

## 5. STOCHASTIC REDUCED-ORDER MODEL

With the calibration process, the uncertainty in weld geometry and weld material properties is lumped into the constitutive model effectively accounting for details of the weld microstructure with the various parameters of the model. In the enrichment process, the available data for those parameters is extended to account for pragmatic limitations in characterization experiments. In the following, we describe a general process to construct an SROM for uncertain data [4, 5]. SROMs are a discrete approximation for a continuous random variable or random vector with samples carefully chosen to preserve their statistics. We note that SROMs are general and can be applied to problems with other uncertain quantities of interest, for example, parametric descriptions of weld microstructure [23].

SROMs provide distinct advantages for our application. We seek to use MCS for estimating the laser weld reliability because it is a broadly applicable uncertainty quantification (UQ) method known to converge for a large class of problems. Further, MCS has available error bounds, e.g., confidence intervals; it remains tractable as the number of random variables grows and it can be implemented in a simple manner that does not require intrusive code rewrites. SROMs enable a surrogate model for weld response, described in Section 6, that is fully dependent on the probability law of the uncertain data and that can be evaluated rapidly during MCS.

### 5.1. Construction of the stochastic reduced-order model

Let  $\Theta$  be a  $d$ -dimensional random vector with known probability. Let  $\tilde{\Theta}$  be another  $d$ -dimensional random vector with samples  $\{\tilde{\theta}_1, \dots, \tilde{\theta}_m\}$ ,  $m \ll n$ . The components of  $\tilde{\Theta}$  correspond to the same physical quantities as the components of  $\Theta$ . The samples of  $\tilde{\Theta}$  are selected from the samples of  $\Theta$  via an optimization algorithm [24] and  $\tilde{\Theta}$  is used to approximate  $\Theta$ . Denote by  $\Gamma$  the range of  $\Theta$ , so that the samples  $\{\tilde{\theta}_k\}$  of  $\tilde{\Theta}$  are in  $\Gamma$ . Let  $\{\Gamma_k\}$ ,  $k = 1, \dots, m$ , be a Voronoi partition of  $\Gamma$  with centers at the samples  $\{\tilde{\theta}_k\}$  of  $\tilde{\Theta}$ . These partitions are situated so that a point  $\theta \in \Gamma$  belongs to  $\Gamma_k$  if its distance to  $\tilde{\theta}_k$  is shorter than to any other samples  $\tilde{\theta}_l$  of  $\tilde{\Theta}$ , that is,  $\|\theta - \tilde{\theta}_k\| < \|\theta - \tilde{\theta}_l\|$ ,  $l \neq k$ . The probability of the samples  $\{\tilde{\theta}_k\}$  are  $p_k = \Pr(\Theta \in \Gamma_k)$ ,  $k = 1, \dots, m$ . The samples  $\{\tilde{\theta}_k\}$  and the corresponding partition  $\{\Gamma_k\}$  of  $\Gamma$  define completely the probability law of  $\tilde{\Theta}$ . For example, the marginal moments of any order  $b \geq 1$ , the marginal distributions, and the correlations of  $\tilde{\Theta}$  are

$$\tilde{\mu}_s(b) = E[\tilde{\Theta}_s^b] = \sum_{k=1}^m p_k (\tilde{\theta}_{k,s})^b, \quad (7a)$$

$$\tilde{F}_s(x) = \Pr(\tilde{\Theta}_s \leq x) = \sum_{k=1}^m p_k 1(\tilde{\theta}_{k,s} \leq x), \quad \text{and} \quad (7b)$$

$$\tilde{c}_{st} = E[\tilde{\Theta}_s \tilde{\Theta}_t] = \sum_{k=1}^m p_k \tilde{\theta}_{k,s} \tilde{\theta}_{k,t}, \quad (7c)$$

where  $\tilde{\Theta}_s$  and  $\tilde{\theta}_{k,s}$  denote coordinates of  $\tilde{\Theta}$  and  $\tilde{\theta}_k$ ,  $1(A)$  denotes the indicator function that is equal to 1 if event  $A$  is true and 0 otherwise, and  $s, t = 1, \dots, d$ .

Any pair  $\{\tilde{\theta}_k, \Gamma_k\}$ ,  $k = 1, \dots, m$ , defines an approximate representation  $\tilde{\Theta}$  for  $\Theta$ . Our objective is to construct a representation that is optimal in some sense for a specified model size  $m$ . The defining parameters of  $\tilde{\Theta}$  are selected to minimize the discrepancy between properties of  $\tilde{\Theta}$  and  $\Theta$ , for example, differences between marginal moments, distributions, and correlation matrices of these two vectors. If the probability law of  $\Theta$  is known, the defining parameters of  $\tilde{\Theta}$  can be selected to minimize an objective function of the form

$$e = \max_{1 \leq b \leq \bar{b}} \max_{1 \leq s \leq d} \alpha_{s,b} |\tilde{\mu}_s(b) - \mu_s(b)| + \max_x \max_{1 \leq s \leq d} \beta_s |\tilde{F}_s(x) - F_s(x)| + \zeta_{s,t} \max_{s,t} |\tilde{c}_{st} - c_{st}|, \quad (8)$$

where  $\mu_s(b) = E[\Theta_s^b]$ ,  $F_s(x) = \Pr(\Theta_s \leq x)$ ,  $c_{st} = E[\Theta_s \Theta_t]$ ,  $\Theta_s$  denotes the  $s$ -component of  $\Theta$ ,  $\bar{b} \geq 1$  is an integer representing the largest marginal moment of interest, and  $\alpha_{s,b}, \beta_s, \zeta_{s,t} > 0$  are weighting factors. The random vector  $\Theta$  that minimizes  $e$  defined by Equation (8) is said to be an SROM for  $\Theta$ .

If the probability law of  $\Theta$  is unknown and information on  $\Theta$  instead consists of  $n$  independent, equally likely samples  $\{\theta_i\}$  of this vector, SROMs  $\tilde{\Theta}$  for  $\Theta$  can be constructed in a similar manner, that is, by minimizing an objective function of the type in Equation (8). The only difference is that

the entries  $\mu_s(r)$ ,  $F_s(x)$ , and  $c_{st}$  in this equation are replaced with their estimators

$$\hat{\mu}_s(b) = \sum_{k=1}^n (1/n) (\theta_{k,s})^b, \quad (9a)$$

$$\hat{F}_s(x) = \sum_{k=1}^n (1/n) \mathbf{1}(\theta_{k,s} \leq x), \quad \text{and} \quad (9b)$$

$$\hat{c}_{st} = \sum_{k=1}^n (1/n) \theta_{k,s} \theta_{k,t}, \quad (9c)$$

where  $\{\theta_{i,s}\}$  denote the components of sample  $\theta_i$ ,  $i = 1, \dots, n$ ,  $s = 1, \dots, d$ .

### 5.2. Stochastic reduced-order model for the enriched laser weld data

We constructed SROMs with  $m = 10, 20, 40$  and  $80$  for the enriched constitutive parameters from Section 4.3. Subsequently, FE calculations were made with the mesh described in Section 3.1 for each parameter set from each SROM and for each of the  $n = 5000$  parameter sets from Section 4.3. Figure 11 plots the FE-computed, force-displacement response for the SROMs on top of those for the enriched data samples. The SROM results are colored by their associated probability  $\{p_k, k = 1, \dots, m\}$  as computed using the partitioning  $\{\Gamma_k\}$  of the SROM. The enriched data

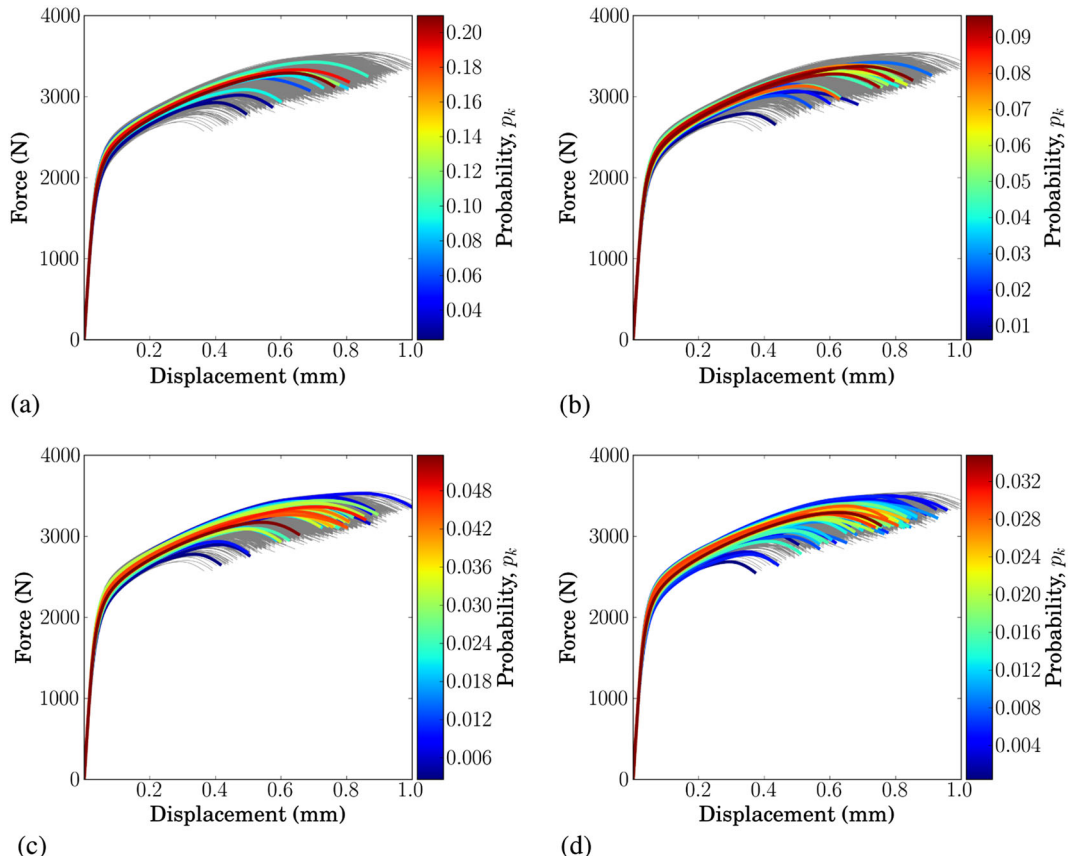


Figure 11. The force-displacement response computed by finite element (FE) calculation for (a) the 10-sample stochastic reduced-order model (SROM), (b) the 20-sample SROM, (c) the 40-sample SROM, and (d) the 80-sample SROM colored by their probabilities and overlaid on the FE calculation for the 5000 enriched samples (gray).

results are plotted underneath in gray. For each SROM, the high probability samples fall in the center of the gray curves and the low probability samples reach outward towards the extremes of the gray curves.

## 6. STOCHASTIC REDUCED-ORDER MODEL-BASED SURROGATE MODEL AND MONTE CARLO SIMULATION

In this section, we outline the construction of an SROM-based surrogate model that provides a piecewise constant or piecewise linear response surface to map samples of  $\Theta$  to a quantity of interest [6]. The surrogate model is proposed to reduce the computational cost of the component simulations. We demonstrate its construction for the force-displacement response of laser welded specimens with uncertain properties subjected to deterministic boundary conditions. Developments are based on SROMs as defined previously and FE solutions for partial differential equations. The proposed method can be viewed as a smart MCS. In contrast to the traditional Monte Carlo that uses a large number of equally likely samples, the proposed method utilizes a small number of samples that may not be equally likely to construct a surrogate model that is subsequently employed to generate output samples. Further, the method is non-intrusive and allows the use of any FE code.

### 6.1. The stochastic reduced-order model-based surrogate

Let  $u \mapsto \Pi(u)$  be the unknown weld response for a specimen with random geometry and material properties under deterministic loading, referred to as the global or specimen weld response, where  $u$  and  $\Pi(u)$  denote a displacement and the corresponding load, respectively. This mapping can be given in the form

$$\Pi(u) = \Pi(u; \Theta), \quad u \geq 0, \quad (10)$$

where  $\Theta$  is the random vector characterizing the uncertainty in material properties and specimen geometry, as previously discussed. Because it depends on a collection of random variables,  $\Pi(u; \Theta)$  in Equation (10) constitutes a parametric stochastic process, i.e., a deterministic function of  $u$  that depends on the random vector  $\Theta$ .

Let  $\{\tilde{\theta}_k, \Gamma_k\}$ ,  $k = 1, \dots, m$ , be the defining parameters of an SROM  $\tilde{\Pi}$  for  $\Theta$ . Two surrogate models are developed for the weld response  $\Pi(u; \Theta)$ . For a fixed  $u$ , they approximate the response surface of  $\Pi(u; \Theta)$  with support equal to the range  $\Gamma$  of  $\Theta$  by piecewise constant and piecewise linear functions over the cells  $\{\Gamma_k\}$  of the Voronoi tessellation in  $\Gamma$ . The models are denoted by  $\tilde{\Pi}(u; \Theta)$  and  $\tilde{\Pi}_L(u; \Theta)$ , respectively, and have the expressions

$$\tilde{\Pi}(u; \Theta) = \sum_{k=1}^m 1(\Theta \in \Gamma_k) \tilde{\pi}_k(u) \quad \text{and} \quad (11a)$$

$$\tilde{\Pi}_L(u; \Theta) = \sum_{k=1}^m 1(\Theta \in \Gamma_k) [\tilde{\pi}_k(u) + \nabla \tilde{\pi}_k(u) \cdot (\Theta - \theta_k^*)], \quad (11b)$$

where  $\tilde{\pi}_k(u) = \Pi(u; \theta_k^*)$  and  $\nabla \tilde{\pi}_k(u) = (\partial \Pi(u; \Theta) / \partial \Theta_1, \dots, \partial \Pi(u; \Theta) / \partial \Theta_d)'|_{(\Theta=\theta_k^*)}$  are the gradients of  $\Pi(u; \Theta)$  at  $\Theta = \theta_k^*$ ,  $k = 1, \dots, m$ . Options for the choice of  $\theta_k^*$  include

$$\theta_k^* = \tilde{\theta}_k \quad \text{or} \quad (12a)$$

$$\theta_k^* = \bar{\theta}_k = E[\Theta | \Theta \in \Gamma_k]. \quad (12b)$$

By Equation (11b), the piecewise linear surrogate  $\tilde{\Pi}_L(u; \Theta)$  approximates the weld response  $\Pi(u; \Theta)$  by hyperplanes tangent to it at  $(\theta_k^*, \tilde{\pi}_k(u))$  over the Voronoi cells  $\{\Gamma_k\}$  for a fixed  $u$  as illustrated in 2-D in Figure 12. The error in this approximation grows as the sample point moves further away from the expansion point. For Voronoi cells that are not equi-axed and whose contents are not evenly distributed, the Voronoi seed  $\tilde{\theta}_k$  may lie far away from other points within the cell.

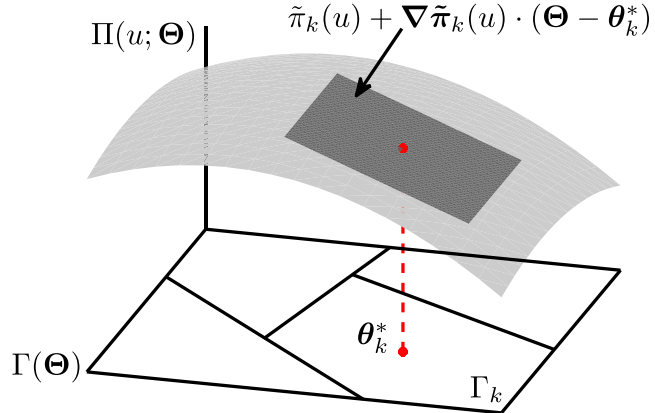


Figure 12. Illustration of sampling a response surface with a hyperplane.

As an alternative to minimize the distance between the expansion point and the samples in a cell, the expansion could be performed about the local mean of the data within a cell as in Equation (12b). It can be shown that  $\tilde{\Pi}_L(u; \Theta)$  converges almost surely to  $\Pi(u; \Theta)$  provided the diameters of the cells  $\{\Gamma_k\}$  vanish as  $m$  increases indefinitely and  $\Pi(u; \Theta)$  is differentiable with respect to the components of  $\Theta$  [6]. Higher-order surrogates can be imagined and are limited only by the differentiability of the quantity of interest and the available compute power.

In summary, once an SROM  $\tilde{\Theta}$  has been obtained for  $\Theta$ , the implementation of the surrogate weld response  $\tilde{\Pi}_L(u; \Theta)$  requires  $m(d + 1)$  deterministic FE calculations where  $d$  denotes the dimension of  $\Theta$  and  $m$  denotes the size of  $\tilde{\Theta}$ , the SROM for  $\Theta$ . The size  $m$  of  $\tilde{\Theta}$  is chosen such that the number of required FE calculations is manageable. Statistics of  $\tilde{\Pi}(u; \Theta)$  are known by the partitioning  $\{\Gamma_k\}$  and the statistics of  $\tilde{\Pi}_L(u; \Theta)$  can be obtained efficiently by MCS because these models are available in closed form. The algorithm for constructing the models in Equation (11), generating samples, and calculating statistics involves the following three steps.

- (1) Construct an SROM  $\tilde{\Theta}$  for  $\Theta$ . Denote by  $\{\tilde{\theta}_k, \Gamma_k\}$ ,  $k = 1, \dots, m$ , the defining parameters of the model.
- (2) Calculate the force-displacement curves  $\{\tilde{\pi}_k(u)\}$  and the gradients  $\{\nabla \tilde{\pi}_k(u)\}$  for  $\tilde{\Pi}_L(u; \Theta)$ .
- (3) Generate samples of  $\Theta$ , calculate corresponding samples of  $\tilde{\Pi}_L(u; \Theta)$ , and estimate properties of the surrogate for  $\Pi(u; \Theta)$ . Note that the Voronoi partition does not have to be constructed explicitly. A sample of  $\Theta$  is allocated to a particular cell depending on its distance to cell centers.

Finite differences can be used to approximate the gradients in step 2. For example,  $\partial \Pi(u; \Theta) / \partial \Theta_j$  can be approximated at  $\Theta = \tilde{\theta}_k$  by  $(\tilde{\pi}_k(u; \tilde{\theta}_k + 1_j \Delta_j) - \tilde{\pi}_k(u; \tilde{\theta}_k)) / \Delta_j$ , where  $1_j$  is an  $d$ -dimensional vector whose components are 0 except for component  $j = 1, \dots, d$ , which is 1. To obtain accurate sensitivities, the perturbations  $\{\Delta_j\}$  need to be sufficiently large such that the differences  $|\tilde{\pi}_k(u; \tilde{\theta}_k + 1_j \Delta_j) - \tilde{\pi}_k(u; \tilde{\theta}_k)|$  are not of the order of discretization errors and sufficiently small such that they capture the local behavior of the solution.

## 6.2. Error bounds for the stochastic reduced-order model-based surrogate

SROMs are constructed to optimally represent the uncertainty in inputs; however, this provides no guarantees that the surrogate constructed from the SROM samples is optimal. Here, we outline bounds for error on the SROM-based surrogate and suggest how this may be applied to locally refine the SROM to improve error in the estimated response. Developments follow [25]. Let  $\Pi_{\text{exact}}(u; \Theta)$ ,  $\Pi_{\text{FE}}(u; \Theta)$ , and  $\tilde{\Pi}(u; \Theta)$ ,  $\tilde{\Pi}_L(u; \Theta)$  be the exact, finite element, and two surrogate solutions,

respectively. The error of, e.g., the surrogate model  $\tilde{\Pi}_L(u; \Theta)$  can be bounded by

$$|\Pi_{\text{exact}}(u; \Theta) - \tilde{\Pi}_L(u; \Theta)| \leq |\Pi_{\text{exact}}(u; \Theta) - \Pi_{\text{FE}}(u; \Theta)| + |\Pi_{\text{FE}}(u; \Theta) - \tilde{\Pi}_L(u; \Theta)| \quad (13)$$

on a sample of  $\Theta$ . Under some conditions, there exists a real-valued function  $g(l) \geq 0$  of the size  $l$  of the FE mesh such that  $|\Pi_{\text{exact}}(u; \Theta) - \Pi_{\text{FE}}(u; \Theta)| < g(l)$  for almost all samples of  $\Theta$  and  $g(l) \rightarrow 0$  as  $l \rightarrow 0$  so that the first term on the right side of the aforementioned inequality can be made as small as desired. Accordingly, we focus on the second term of Equation (13).

A general bound on the error  $|\Pi_{\text{FE}}(u; \Theta) - \tilde{\Pi}_L(u; \Theta)|$  can be found in [25]. For simplicity, we illustrate the construction of this bound for the special case in which  $\Theta$  has dimension one and use the notation  $\Pi(u; \Theta) := \Pi_{\text{FE}}(u; \Theta)$ . If there exists  $M > 0$  such that  $\Pr(\max_{\Theta \in \Gamma} |\partial^2 \Pi(u; \Theta)/\partial \Theta^2| < M) = 1$ , then

$$|\Pi(u; \Theta) - \tilde{\Pi}_L(u; \Theta)| \leq \frac{M}{2} \sum_{k=1}^m 1(\Theta \in \Gamma_k) (\Theta - \theta_k^*)^2 \quad (14)$$

for almost all samples of  $\Theta$ . This result can be used to calculate statistics of the surrogate error. For example, we have

$$\mathbb{E}[|\Pi(x; \Theta) - \tilde{\Pi}_L(x; \Theta)|] \leq \frac{M}{2} \sum_{k=1}^m \int_{\Gamma_k} (\theta - \theta_k^*) dF(\theta), \quad (15)$$

where  $F$  denotes the distribution of  $\Theta$  and  $\mathbb{E}[\cdot]$  denotes the expectation operator.

The bound in Equation (14) follows from the observation that the surrogate model consists of local first order Taylor expansions of the solution  $\Pi(x; \Theta)$  in the cells  $\{\Gamma_k\}$  of the Voronoi partition of  $\Gamma$ . For an arbitrary cell  $\Gamma_k$ , there exists  $\theta_{k,0} \in \Gamma_k$  such that

$$\Pi(x; \Theta) = \Pi(x; \theta_k^*) + \frac{\partial \Theta(x; \Theta)}{\partial \Theta} \Big|_{\{\Theta=\theta_k^*\}} (\Theta - \theta_k^*) + \frac{1}{2} \frac{\partial^2 \Theta(x; \Theta)}{\partial \Theta^2} \Big|_{\{\Theta=\theta_{k,0}\}} (\Theta - \theta_k^*)^2 \quad (16)$$

by the Taylor theorem with remainder [26, Theorem 21.1]. This implies

$$\begin{aligned} \left| \Pi(x; \Theta) - \left( \Pi(x; \theta_k^*) + \frac{\partial \Theta(x; \Theta)}{\partial \Theta} \Big|_{\{\Theta=\theta_k^*\}} (\Theta - \theta_k^*) \right) \right| &\leq \left| \frac{1}{2} \frac{\partial^2 \Theta(x; \Theta)}{\partial \Theta^2} \Big|_{\{\Theta=\theta_{k,0}\}} (\Theta - \theta_k^*)^2 \right| \\ &\leq \frac{M}{2} (\Theta - \theta_k^*)^2, \quad \Theta \in \Gamma_k, \end{aligned} \quad (17)$$

which yields the stated bound. We note that the bound in Equation (14) depends on the size of the Voronoi cells, the rate of change of the solution with  $\Theta$ , and the distribution of  $\Theta$ . Equation (17) can be used to choose cells in the current SROM partition that could be refined to improve accuracy [25].

### 6.3. Application of the surrogate to the laser weld

For verification of the solutions from the surrogate model, the enriched data from Section 4 were used with the FE mesh presented in Section 3 to produce 5000 samples of the force-displacement curve  $\Pi(u; \Theta)$ . This illustrates the traditional MCS of the weld response. We refer to this approach as brute force MCS, which is tractable in this case because the ‘component’ model is relatively small. For general complex engineering problems, brute force Monte Carlo is intractable. Subsequently, the algorithm proposed earlier was used to construct a 10-sample SROM and a piecewise-linear surrogate model that was evaluated with the 5000 enriched samples. This requires only  $m(d + 1) = 10(3 + 1) = 40$  FE calculations. We refer to this approach as smart MCS.

Figure 13 plots the brute force MCS response data in red on top of the smart MCS predictions from the surrogate in blue. For a surrogate with no error, each red curve would cover the blue curve for a corresponding sample  $\theta_k$ . In fact, in this example with  $\theta_k^* = \tilde{\theta}_k$ , there are at least 10 curves that overlap exactly, one for each SROM sample. The results in the figure show good agreement

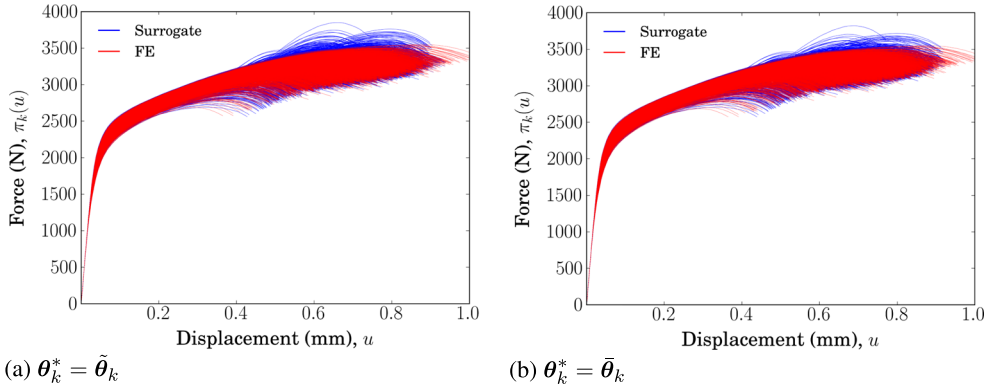


Figure 13. The force-displacement response computed by finite element (FE) calculation (red) and by the 10-sample SROM-based surrogate (blue) for the 5000 samples of  $\Theta$ , using the two choices for  $\theta_k^*$  defined by Equation (12). SROM, stochastic reduced-order model.

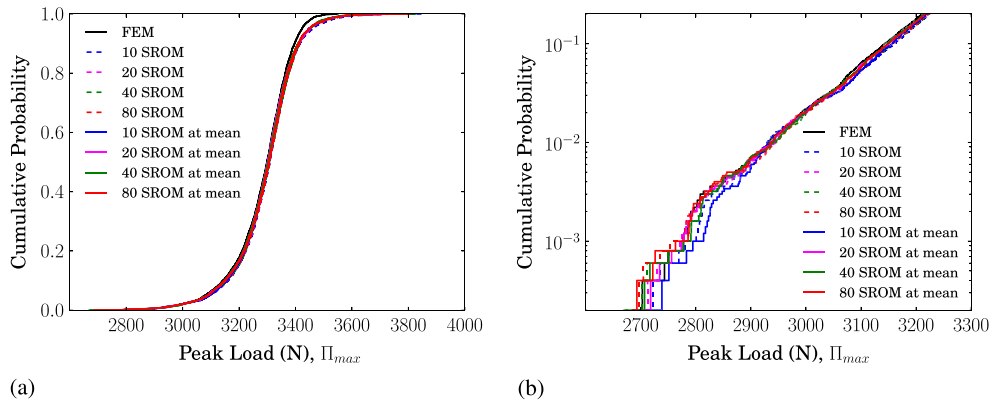


Figure 14. The cumulative distribution of peak load  $\Pi_{max}$  predicted by Monte Carlo simulation with finite element calculations and with the SROM-based surrogate models. (a) Shows the full range of the cumulative distribution while (b) focuses on the lower tail of the distribution with logarithmic scale. SROM, stochastic reduced-order model.

between the surrogate and FE calculations for the majority of the 5000 samples with significant overlap of the red and blue curves. In Figure 13(a), the choice of  $\theta_k^* = \tilde{\theta}_k$  from Equation (12a) was used while Figure 13(b) used  $\theta_k^* = \bar{\theta}_k$  from Equation (12b). Evidently, using the cell averages in the Taylor approximation improves the predictions of peak load as there are fewer false peaks above the brute force data. These false peaks are a result of the Taylor approximation when the distance between  $\theta_k^*$  and a sample  $\theta_i$  of  $\Theta$  becomes large, which is the dominant source of error in the surrogate. Further exploration of the impact of this is outlined in the succeeding sections, e.g., see Equation (18a) and the discussion surrounding it.

Figure 14 illustrates the CDF of peak force  $\Pi_{max} = \max_u \Pi(u; \Theta)$  predicted by MCS with FE calculations and by MCS with the SROM-based surrogate models for  $m = 10, 20, 40$  and  $80$  and both options for  $\theta_k^*$  from Equation (12). For lack of an analytical solution for the CDF of peak load for the welded coupon, the brute force estimate is assumed to be the ‘truth’ solution. In Figure 14(a), the full range of the cumulative distribution is plotted. The surrogate model performs well with small but noticeable differences from the FE calculations above 3330 N. However, these are acceptable because the focus here is on the prediction of failure, which corresponds with the distribution’s lower tail. These differences are caused by the false peaks in the data and investigated further in the succeeding sections. There is very little observable difference between the various surrogate model predictions. Figure 14(b) focuses on the lower tail of the distribution where below-average behavior leads to failure at lower loads. From this plot, the FE-computed critical load for a probability of

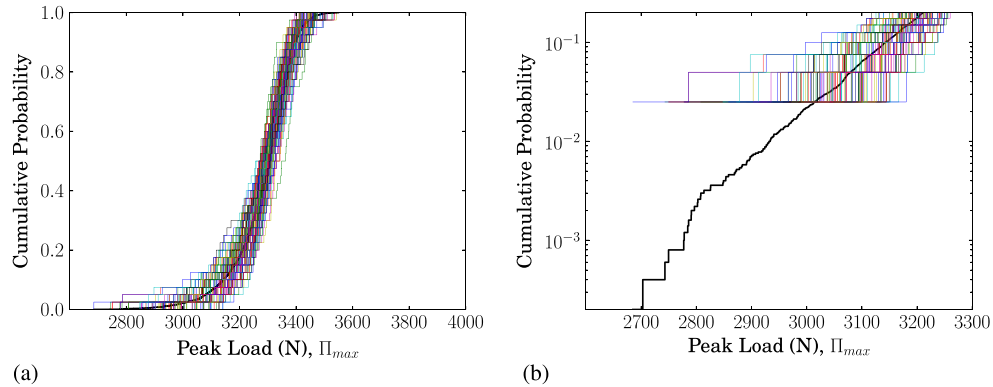


Figure 15. The cumulative distribution of peak load  $\Pi_{max}$  predicted by 100 sets of 40 samples of finite element (FE) calculations (colored lines) and compared with 5000 FE calculations (black line). (a) Shows the full range of the cumulative distribution while (b) focuses on the lower tail of the distribution with logarithmic scale.

Table I. Computational expense in CPU seconds.

	Construct SROM*	FE calculations **	Evaluate surrogate*	Total
Brute force MCS	n.a.	33,400,000 (5000 FE calculations)	n.a.	33 400 000
10 SROM at mean	948	511 000 (40 FE calculations)	6.69	512 000

\*Intel ® Xeon ® x5675 CPU @ 3.07 GHz w/ 48 GiB RAM

\*\*Intel ® Nehalem ® x5570 CPU @ 2.93 GHz w/ 1.5 GiB RAM

SROM, stochastic reduced-order model; MCS, Monte Carlo simulation; FE, finite element, CPU, central processing unit.

failure of 0.025 was 3014 N. With the surrogate models, the critical load can be estimated between 3016 to 3025 N, a relative difference of 0.06% and 0.3%, respectively.

Brute force MCS with FE calculations was conducted with sample sizes of 40, equivalent in computational work to constructing the 10-sample, SROM-based surrogate. Figure 15 illustrates the predicted cumulative distribution of peak load for 100 sets of 40 samples plotted on top of the FE-computed CDF from the full set of 5000 samples. The purpose of this plot is to illustrate that, for identical computational cost, the proposed approach is vastly superior to traditional brute force Monte Carlo. The data clearly has a wider range than the predictions from the surrogate model with some sets more accurate than others. Figure 15(b) again focuses on the lower tail of the distribution. From this, the critical load for a probability of failure of 0.025 has a significantly wider estimate from 2184 to 3166 N, a relative difference ranging from 5% to 28%, and no estimates can be made for lower probabilities of failure. Further, in practice, when the ‘truth’ solution is unavailable, the confidence bounds associated with 40 samples are large. Table I reports the computational cost in CPU seconds of the brute force MCS versus smart MCS. Note, the cost associated with building the SROM and sampling the surrogate model is small compared with the cost of the 40 FE-calculations required to construct the surrogate. For the illustration in this paper, the cost of brute force MCS at 33 444 036 CPU seconds is 65 times greater than the surrogate model. For components of practical interest, the cost of brute force MCS is intractable.

Figure 16 illustrates the CDF from the brute force MCS and the 10-sample SROM-based surrogate model, plotted against the CDF constructed from the original 40 experimental test coupons that were used for calibration in Section 3. Broadly speaking, and considering the relatively few data points from experiment, the computed results agree well with the measured result.

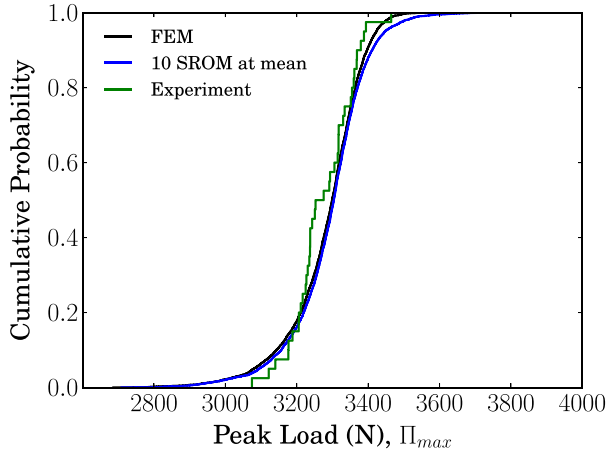


Figure 16. The cumulative distribution of peak load  $\Pi_{max}$  constructed from the brute force Monte Carlo simulation, the 10-sample SROM-based surrogate with  $\theta_k^* = \bar{\theta}_k$ , and the 40 experimental weld coupons. SROM, stochastic reduced-order model; FEM, finite element model.

To further investigate the performance of the surrogate, several difference measures were computed for each sample as

$$D_0 = \|\boldsymbol{\Theta} - \boldsymbol{\theta}_k^*\|_2, \quad (18a)$$

$$D_1 = \frac{\max(\Pi(u)) - \max(\tilde{\Pi}_L(u))}{\max(\Pi(u))}, \quad \text{and} \quad (18b)$$

$$D_2 = \frac{\int_0^{u_f} (\Pi(u)) - \tilde{\Pi}_L(u) du}{\int_0^{u_f} (\Pi(u)) du} \quad (18c)$$

where  $\Pi(u)$  represents the uncertain force-displacement response as computed by FE calculation and  $\tilde{\Pi}_L(u)$  represents the force-displacement response computed by the surrogate Equation (11b). Equation (18a) computes distance between the point chosen for the Taylor expansion and the Monte Carlo sample. Equation (18b) computes the relative difference between the predicted peak loads corresponding to weld failure. It is possible that predicted peak loads agree but the remainder of the surrogate-predicted response be significantly erroneous, e.g., the strain at peak load could differ dramatically. Equation (18c) gives an alternate measure by computing the difference in energy dissipation normalized by the FE-computed energy dissipation. For this, the data were manipulated to have the same displacement domain, and discretization in  $u$  and the data were truncated when the load had been shed to 95% of the peak value. In cases where a displacement point fell beyond the truncated force values, the displacement was assigned zero force.

Figure 17 plots histograms from the results of Equation (18) with  $\theta_k^* = \tilde{\theta}_k$  on the left and  $\theta_k^* = \bar{\theta}_k$  on the right. From the top row in the figure, the number of samples in the range 15 000 - 20 000 is reduced and the mean distance appears to be shifted towards zero when  $\theta_k^* = \bar{\theta}_k$ ; however, there are some samples that end up further away. The histograms corresponding to difference in peak load (middle) look very similar with the mean near zero and most of the data within 10% of the FE-computed peak load. There are certain extreme values near -0.3 that appear to be removed in Figure 17(b) as a result of using  $\bar{\theta}_k$ . The histogram corresponding with Equation (18c) has a long tail in the positive range as a result of filling out-of-range displacements with zero during the interpolation process described earlier. Again, however, the relative differences appear to have a mean near zero with small improvements in the extreme values.

The difference metrics assist in isolating two cases for closer evaluation. First, there are several data in Figure 13(a) that show obviously high predictions of peak load with considerable improvement, evident by inspection of Figure 13(b). The sample  $\theta_{3689}$  illustrates one such case where

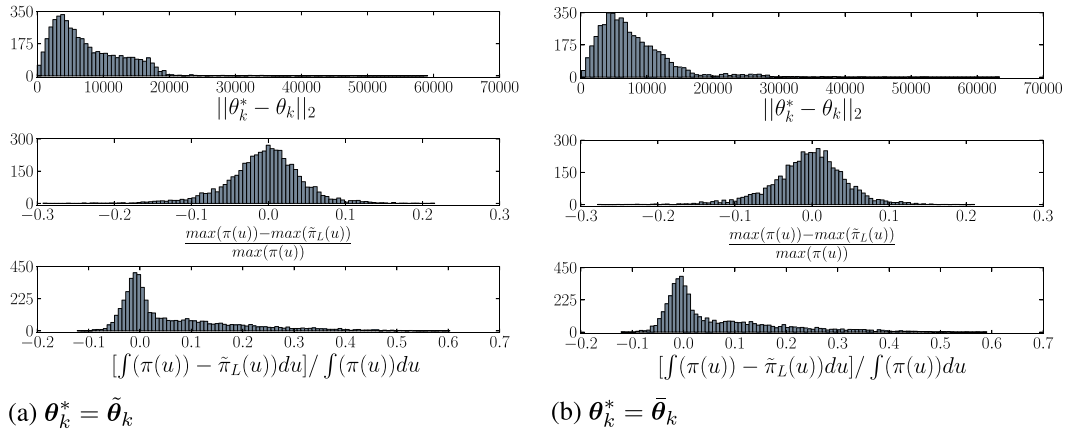


Figure 17. Histograms of the difference measures from Equation (18) for the piecewise-linear surrogate  $\tilde{\Pi}_L$  defined by Equation (11b) with (a)  $\theta_k^* = \tilde{\theta}_k$  on the left and (b)  $\theta_k^* = \bar{\theta}_k$  on the right.

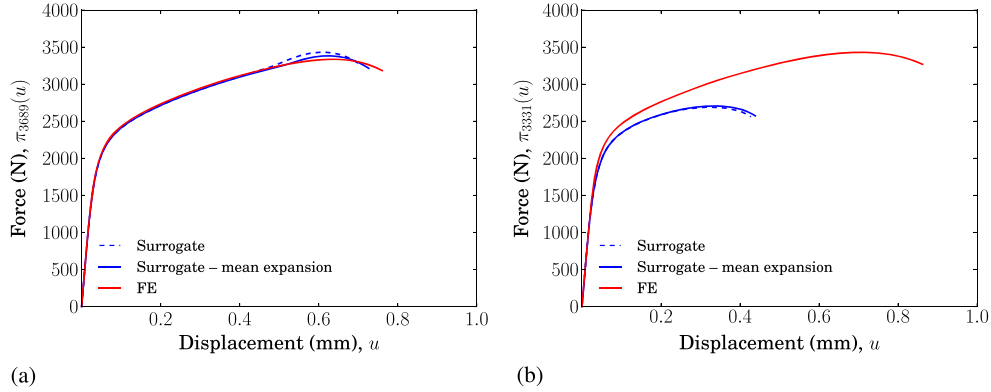


Figure 18. (a) A force-displacement plot for a sample improved by using  $\theta_k^* = \bar{\theta}_k$  and (b) a force-displacement plot for a sample where the surrogate performs poorly.

$\|\tilde{\theta}_{3689} - \theta_{3689}\|_2 = 7760.5$  and  $\|\bar{\theta}_{3689} - \theta_{3689}\|_2 = 5546.1$ . The force-displacement for this sample is plotted in Figure 18(a) showing improvement in both the predicted peak load and the shape of the force-displacement curve. For this sample,  $d_1$  improved from  $-0.0285$  to  $-0.0136$  and  $d_2$  improved from  $0.0781$  to  $0.0515$ . Figure 18(b) plots sample  $\theta_{3331}$ , which is an example of poor performance from the surrogate. For this sample,  $\|\tilde{\theta}_{3331} - \theta_{3331}\|_2 = 48215.4$  and  $\|\bar{\theta}_{3331} - \theta_{3331}\|_2 = 52394.5$ , actually increasing with  $\theta_k^* = \theta_k$ . Despite this increase, the difference measures, while quite large, improved from  $0.2157$  to  $0.2109$  and  $0.6032$  to  $0.5904$  for  $d_1$  and  $d_2$ , respectively. Overall, despite the obvious improvements in Figure 13, the measurable benefits of using  $\theta_k^* = \theta_k$  seem to be low. This, however, will be revisited in the succeeding sections during assessment of the statistics of predicted peak force.

Table II lists the moments up to order 6 as computed by Equation (9a) for the data from the brute force MCS and the surrogate models corresponding to 10-sample and 80-sample SROMs and includes their relative differences computed as

$$D_3 = 100 * \frac{E\left[(\Pi(u; \Theta))^b\right] - E\left[(\tilde{\Pi}_L(u; \Theta))^b\right]}{E\left[(\Pi(u; \Theta))^b\right]}, b = 1, \dots, 6 \quad (19)$$

where  $\Pi(u; \Theta)$  is approximated with the brute force MCS results. The accuracy is remarkable with differences ranging from 0.31% up to 3.2%. Notably, the accuracy improves in every case for  $\theta_k^* = \bar{\theta}_k$ .

Table II. Moment estimators to order = 6 for peak force computed from Equation (9a) with percent difference  $d_3$  from Equation (19). Units are  $N^b$ ,  $b = 1, \dots, 6$ .

	Moment order					
	1	2	3	4	5	6
FE	3.28e+03	1.08e+07	3.54e+10	1.17e+14	3.84e+17	1.27e+21
SROM size						
$\theta_k^* = \bar{\theta}_k$						
10	3.3e+03	1.09e+07	3.6e+10	1.19e+14	3.95e+17	1.31e+21
( $d_3$ )	(-0.492%)	(-1.002%)	(-1.530%)	(-2.078%)	(-2.648%)	(-3.242%)
80	3.3e+03	1.09e+07	3.59e+10	1.19e+14	3.93e+17	1.3e+21
( $d_3$ )	(-0.438%)	(-0.891%)	(-1.359%)	(-1.844%)	(-2.346%)	(-2.868%)
$\theta_k^* = \bar{\theta}_k$						
10	3.29e+03	1.08e+07	3.58e+10	1.18e+14	3.91e+17	1.29e+21
( $d_3$ )	(-0.314%)	(-0.638%)	(-0.972%)	(-1.319%)	(-1.679%)	(-2.054%)
80	3.29e+03	1.08e+07	3.58e+10	1.18e+14	3.91e+17	1.29e+21
( $d_3$ )	(-0.313%)	(-0.640%)	(-0.983%)	(-1.342%)	(-1.718%)	(-2.113%)

FE, finite element; SROM, stochastic reduced-order model.

## 7. REMARKS

We view this methodology as more widely applicable than our example demonstrates. Foremost, it is envisioned that, in practice, the component will be a much larger body that contains elements represented by the sub-component, e.g., laser welds. SROMs and surrogates can be constructed for many other sources of uncertainty, e.g., bolted connections, adhesives, boundary conditions, environmental conditions, manufacturing defects, and manufacturing tolerances. Further, SROMs and their surrogates are general enough to be extended to other mechanics disciplines, e.g., fluid, thermal, radiation, and they have the advantage of minimally invasive implementation without requiring code rewrites.

Our reference to the brute force MCS estimate as the ‘truth’ solution and its favorable comparison with the SROM-based CDF requires further comment. The smart MCS approach results in high fidelity reliability predictions with minimal computational effort, but the accuracy of both MCS methods are subject to the fidelity of the available data. Given the same data, smart MCS wins in terms of performance. However, in the absence of sufficient data, neither method produces accurate results. Ideally, the analyst has sufficient data that the enrichment process can be conducted with significant confidence. This is not a short coming of our methodology; rather, obtaining sufficient data is a common engineering challenge.

## 8. SUMMARY & CONCLUSIONS

The objective of this work was to provide a rational and tractable engineering solution to the problem of predicting structural reliability of a laser welded component. The fundamental premise was that traditional MCS is intractable because of the cost of the computational model for the component. We illustrated our methodology by computing the probability of failure for a laser welded tensile coupon constructed from 304L SS. In the absence of our methodology, the analyst would calibrate a constitutive model to experimental data that characterizes the material behavior. This would be used in an FE model to predict residual strength given some details on loading and environment. Variability of the material behavior might be accounted for by running several FE calculations with bounding material properties.

In contrast, with our methodology, calibration was performed to experimental data characterizing the failure of a sub-component. This calibration was performed with an FE model designed to behave well, capture the dominant mechanism, and represent the resolution of the component FE model. Without a rich set of data to characterize the uncertainty in support of the calibration, we

presented a method to enrich the data. An SROM was constructed that discretely represented the uncertain inputs, with sample-probability pairs carefully chosen to preserve certain properties of the data. From the SROM, a surrogate for the component FE calculations was constructed. The surrogate was subsequently used in MCS to generate samples of the component response that were used to estimate the component reliability. The surrogate was much less computationally expensive to construct and sample than the brute force MCS of comparable accuracy. Further, the surrogate was far more accurate than the brute force MCS of comparable computational expense.

We illustrated our methodology with a verification problem that computed reliability for the sub-component, i.e., the surrogate model was constructed for the same FE model used for calibration. The predictions from the surrogate provided accurate estimates when compared with the brute force MCS and the experimental results. Our example demonstrated that

- Calibration can be used to lump uncertainties into a simple constitutive model;
- Enrichment through a non-Gaussian translation model can extend limited data to a robust set;
- SROMs provided efficient reduction of the stochastic space;
- The SROM-based surrogate model was 65 times faster than the brute force MCS for 5000 samples with equivalent accuracy;
- Brute force MCS with comparable computational cost to the SROM-based surrogate is less accurate, has lower confidence bounds, and provides no data for probabilities of the lower tail; and
- The method is self-consistent and compares well with the CDF constructed from the original 40 experimental samples.

## NOMENCLATURE

$1(A)$	Indicator function on $A$
$\Gamma_k$	$k^{\text{th}}$ Voronoi partition
$\Theta$	Random vector with coordinates $\Theta_1 = Y$ , $\Theta_2 = R$ , and $\Theta_3 = H$
$\tilde{\Theta}$	SROM for $\Theta$ with coordinates $\tilde{\Theta}_1$ , $\tilde{\Theta}_2$ , and $\tilde{\Theta}_3$
$\Theta_s, \tilde{\Theta}_s$	$s$ component of the random vectors $\Theta$ and $\tilde{\Theta}$
$\Pi(u)$	Force-displacement response of weld
$\Phi$	CDF of the standard Gaussian random variable
$\theta_k, \tilde{\theta}_k$	$k^{\text{th}}$ deterministic sample of $\Theta$ and $\tilde{\Theta}$
$\theta_{k,s}, \tilde{\theta}_{k,s}$	$s$ component of the $k^{\text{th}}$ deterministic sample of $\Theta$ and $\tilde{\Theta}$
$\mu_s$	Mean of $\Theta_s$
$\xi_{kl}$	Elements of covariance matrix of $\Theta$
$\rho_{kl}$	Elements of covariance matrix of $G$
$E(A)$	Expectation of $A$
$F_k$	Marginal CDF of $\Theta_k$
$G$	Gaussian random vector with coordinates $G_k$
$h, H$	Deterministic and random hardening term
$\Pr(A)$	Probability of $A$
$r, R$	Deterministic and random recovery term
SROM	Stochastic reduced-order model
$\text{Var}[A]$	Variance of $A$
$y, Y$	Deterministic and random initial yield strength
$c_{st}$	Elements of correlation matrix of $\Theta$
$d$	Dimension of $\Theta$
$f_k$	Deterministic nonlinear mapping applied to $G_k$
$l$	Finite element mesh size
$m$	Number of samples in the SROM
$n$	Number of samples in enriched data set
$q$	Number of experiments

## ACKNOWLEDGEMENTS

Sandia National Laboratories is a multi-program laboratory managed and operated by Sandia Corporation, a wholly owned subsidiary of Lockheed Martin Company, for the US Department of Energy National Nuclear Security Administration under contract DE-AC04-94AL85000.

## REFERENCES

1. Miyamoto I, Knorovsky GA. Laser micro welding. In *Microjoining and Nanojoining*, Zhou Y (ed.). Woodhead Publishing Limited: Abingdon Hall, Abingdon, Cambridge, CB21 6AH, England, 2008; 345–417.
2. Boyce BL, Reu PL, Robino CV. The constitutive behavior of laser welds in 304L stainless steel determined by digital image correlation. *Metallurgical and Materials Transactions A* 2006; **37A**:2481–2492.
3. Madison JD, Aagesen LK. Quantitative characterization of porosity in laser welds of stainless steel. *Scripta Materialia* 2012; **67**:783–786.
4. Grigoriu MD. Reduced order models for random functions. Application to stochastic problems. *Applied Mathematical Modelling* 2009; **33**:161–175.
5. Grigoriu MD. Linear random vibration by stochastic reduced-order models. *International Journal for Numerical Methods in Engineering* 2010; **82**:1537–1559.
6. Grigoriu MD. A method for solving stochastic equations by reduced order models and local approximations. *Journal of Computational Physics* 2012; **231**(19):6495–6513.
7. Bamman DJ, Chiesa ML, Johnson GC. Modeling large deformation and failure in manufacturing processes. In *Theoretical and Applied Mechanics*, Tatsumi T, Watanabe E, Kambe T (eds). Elsevier Science, 1996.
8. Brown AA, Bamman DJ. Validation of a model for static and dynamic recrystallization in metals. *International Journal of Plasticity* 2012; **32–33**(0):17–35.
9. Arwade S. Translation vectors with non-identically distributed components. *Probabilistic Engineering Mechanics* 2005; **20**(2):158–167.
10. Aquino W. An object-oriented framework for reduced-order models using proper orthogonal decomposition. *Computer Methods in Applied Mechanics and Engineering* 2007; **196**(4375–4390).
11. Chinesta F, Ladeveze P, Cueto E. A short review on model order reduction based on proper generalized decomposition. *Archives on Computational Methods in Engineering* 2011; **18**(4):395–404.
12. Babuška I, Nobile F, Tempone R. A stochastic collocation method for elliptic partial differential equations with random input data. *SIAM Journal on Numerical Analysis* 2007; **45**(3):1005–1034.
13. Nobile F, Tempone R, Webster CG. A sparse grid stochastic collocation method for partial differential equations with random input data. *SIAM Journal on Numerical Analysis* 2008; **46**(5):2309–2345.
14. Field, Jr. RV, Grigoriu MD, Emery JM. On the efficacy of stochastic collocation, stochastic Galerkin, and stochastic reduced order models for solving stochastic problems. *Probabilistic Engineering Mechanics* in review.
15. SIERRA Solid Mechanics Team. Adagio 4.18 User's Guide. *Technical Report SAND2010-6313*, Sandia National Laboratories: Albuquerque, NM, 2010.
16. de Borst R. Damage, material instabilities, and failure. In *Encyclopedia of Computational Mechanics*, Stein E, de Borst R, Hughes TJR (eds). John Wiley & Sons, Ltd.: New York, 2004; 335–373.
17. Adams BM, Bohnhoff WJ, Dalbey KR, Eddy JP, Eldred MS, Gay DM, Haskell K, Hough PD, Swiler LP. DAKOTA, a multilevel parallel object-oriented framework for design optimization, parameter estimation, uncertainty quantification, and sensitivity analysis: Version 5.0 user's manual. *Sandia Technical Report SAND2010-2183*, Sandia National Laboratories: Albuquerque, NM, 2010.
18. Grigoriu MD. *Applied Non-gaussian Processes: Examples, Theory, Simulation Linear Random Vibration and Matlab Solutions*. Prentice Hall: Englewood Cliffs, NJ, 1995.
19. Field, Jr. RV, Grigoriu MD. Model selection for a class of stochastic processes or random fields with bounded range. *Probabilistic Engineering Mechanics* 2009; **24**(3):331–342.
20. Johnson NL, Kotz S, Balakrishnan N. *Continuous Univariate Distributions*, Vol. 2. Wiley: New York, 1994.
21. Johnson NL, Kotz S, Balakrishnan N. *Continuous Univariate Distributions*, Vol. 1. Wiley: New York, 1994.
22. Keeping ES. *Introduction to Statistical Inference*. Dover: Mineola, 1995.
23. Emery JM, Field, Jr. RV, Grigoriu MD. Stochastic reduced-order models for uncertain geometry of laser welds. *Technical Report SAND2014-xxxx*, Sandia National Laboratories: Albuquerque, NM, in preparation.
24. Warner JE, Grigoriu MD, Aquino Wilkins. Stochastic reduced order models for random vectors: application to random eigenvalue problems. *Probabilistic Engineering Mechanics* 2013; **31**:1–11.
25. Grigoriu MD. Response statistics for random heterogeneous microstructures. *SIAM Journal on Uncertainty Quantification* 2014; **2**:252–275.
26. Brabec RL. *Introduction to Real Analysis*. PWS-KENT Publishing Company: Boston, 1990.